Development of TiAu TES x-ray calorimeters for the X-IFU on ATHENA space observatory

P. Khosropanah, E. Taralli, L. Gottardi, C. P. de Vries, K. Nagayoshi, et al.

P. Khosropanah, E. Taralli, L. Gottardi, C. P. de Vries, K. Nagayoshi, M. L. Ridder, H. Akamatsu, M. P. Bruijn, J.-R. Gao, "Development of TiAu TES x-ray calorimeters for the X-IFU on ATHENA space observatory ," Proc. SPIE 10699, Space Telescopes and Instrumentation 2018: Ultraviolet to Gamma Ray, 106991M (6 July 2018); doi: 10.1117/12.2313439

Event: SPIE Astronomical Telescopes + Instrumentation, 2018, Austin, Texas, United States

Development of TiAu TES X-ray calorimeters for the X-IFU on ATHENA space observatory

P. Khosropanah[1], E. Taralli[1], L. Gottardi[1], C.P. de Vries[1] , K. Nagayoshi[1],
M.L. Ridder[1], H. Akamatsu[1], M.P. Bruijn[1], J.-R. Gao[1,2]

[1]SRON Netherlands Institute for Space Research, Utrecht, the Netherlands
[2]Kavli Institute of Nanoscience, Delft University of Technology, Delft, the Netherlands

ABSTRACT

SRON is developing X-ray transition edge sensor (TES) calorimeters arrays, as a backup technology for X-IFU instrument on the ATHENA space observatory. These detectors are based on a superconducting TiAu bilayer TES with critical temperature of 100 mK on a 1 µm thick SiN membrane with Au or Au/Bi absorbers. Number of devices have been fabricated and measured using a Frequency Division Multiplexing (FDM) readout system with 1-5 MHz bias frequencies. We measured IV curves, critical temperature, thermal conductance, noise and also X-ray energy resolution at number of selected bias points. So far our best calorimeter shows 3.9 eV X-ray resolution at 6 keV. Here we present a summary of our results and the latest status of development of X-ray calorimeters at SRON.

Keywords: ATHENA, X-IFU, transition edge sensor, TES arrays, calorimeters, X-ray spectrometer, SiN membrane.

1. INTRODUCTION

ATHENA [1] is the second 'large mission' of ESA's Cosmic Vision-programme to study astrophysical phenomena near black holes and neutron stars. The X-ray Integral Field Unit (X-IFU) [2] is one of the two instruments on board to deliver spatially resolved high-resolution X-ray spectroscopy over a limited field of view.

While NASA's Goddard Space Flight Center is assigned to deliver the detectors, SRON is also developing X-ray TES calorimeters arrays, as a backup technology for X-IFU, that requires arrays of nearly 4000 detectors, sensitive in 0.2-12 keV energy range with 2.5 eV energy resolution below 7 keV. Our TESes are based on a superconducting TiAu bilayer TES with critical temperature of around 100 mK on a 1 µm thick SiN membrane with Au or Au/Bi absorbers. Number of devices have been successfully fabricated and characterized with a large variety of design parameters, including: TESes with different size and normal resistance, with or without metallic bars, with or without slots in the membrane and variety of absorbers and absorber couplings.

We use an 18-channel Frequency Division Multiplexing (FDM) readout system with 1-5 MHz bias frequencies, which is a small version of the baseline readout system for X-IFU. Characterization is done by measuring the IV curves, critical temperature, thermal conductance and noise. We also measure the X-ray energy resolution using Fe-55 source at 6 keV at selected bias points.

*P.Khosropanah@sron.nl; phone +31 88777 5682; fax +31 88777 5601; sron.nl

Space Telescopes and Instrumentation 2018: Ultraviolet to Gamma Ray, edited by Jan-Willem A. den Herder, Shouleh Nikzad, Kazuhiro Nakazawa, Proc. of SPIE Vol. 10699, 106991M · © 2018 SPIE
CCC code: 0277-786X/18/$18 · doi: 10.1117/12.2313439

2. ARRAY DESCRIPTION

There are quite a few TES calorimeters that are fabricated in SRON with large variation in design parameters such as TES size, thermal conductance (*G*), wiring types and different metallic structures on the TES for excess noise mitigation. In order to make fast steps toward favorable design, chip 6b with the largest variety of TESes was chosen for the test. The schematic picture of this array is shown in Fig. 1 and the description of the each pixel is given in Table 1.

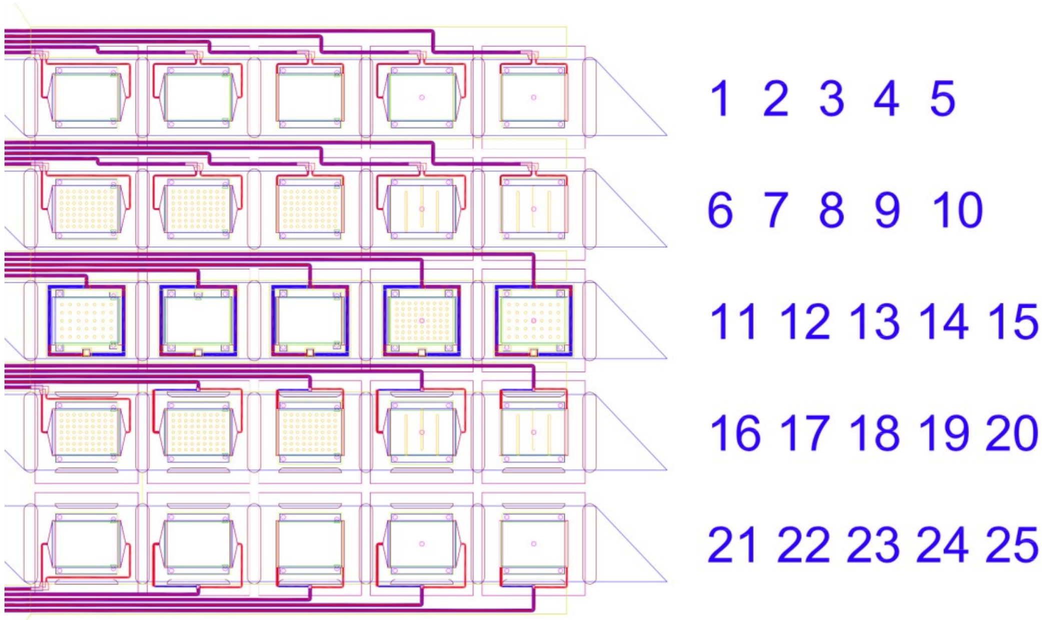

Fig. 1. Schematic picture of the array (chip 6b) with the most diverse design collection.

Table 1. Description of the design variation for chip 6b. *F* is the ratio of the TES that is covered by metallic structures.

1 High-G Bare TES 4 points absorber	2 High-G Bare TES 4 points absorber	3 High-G Bare TES 4 points absorber	4 High-G Bare TES 5 points absorber	5 High-G Bare TES 5 points absorber
6 High-G 7x9 dots, 6 μm Ø F = 0.127 4 points absorber	7 High-G 7x9 dots, 6 μm Ø F = 0.127 4 points absorber	8 High-G 7x9 dots, 6 μm Ø F = 0.127 4 points absorber	9 High-G 3 strips, 5 μm wide 90% of TES width 5 point absorber	10 High-G 3 strips, 5 μm wide 90% of TES width 5 point absorber
11 High-G 5x7 dots, 6 mu Ø F = 0.071 4 points absorber	12 High-G Bare TES 4 points absorber	13 High-G Bare TES 4 points absorber	14 High-G 7x9 dots, 6 μm Ø F = 0.127 5 points absorber	9 High-G 5x7 dots, 6 μm Ø F = 0.071 5 points absorber
16 Low-G As pixel 6	17 Low-G As pixel 7	18 Low-G As pixel 8	19 Low-G As pixel 9	20 Low-G As pixel 5
21 Low-G As pixel 1	22 Low-G As pixel 2	23 Low-G As pixel 3	24 Low-G As pixel 4	25 Low-G As pixel 5

In addition to the design parameters mentioned in Table 1, there are differences in the wiring (see Fig.1). Especially the central row (11 to 15) in the stripline process is dedicated to make the looped return version to minimize the effect of the self-magnetic field as shown in Fig. 2.

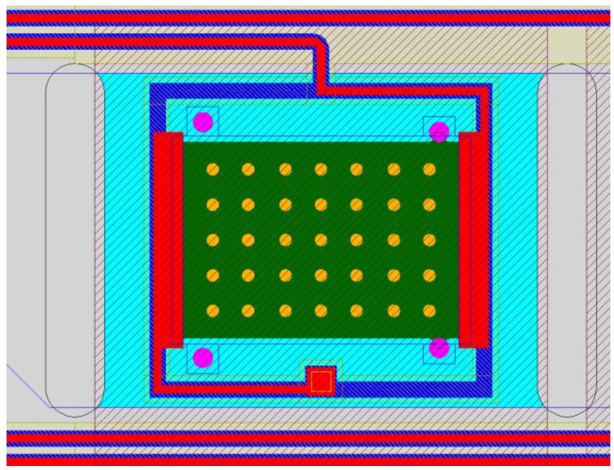

Fig. 2. Schematic picture of TES-13 on the array with special looped return version of the stripline wiring. to minimize the effect of the self magnetic field.

Eight devices were wired for this mmeasurement run as indicated in Fig. 3. The only parameters that are not changing among these calorimeters are the TES size and the absorber. All devices are characterized using an FDM readout system with bias frequencies ranging from 1-5 MHz.

(a) (b)

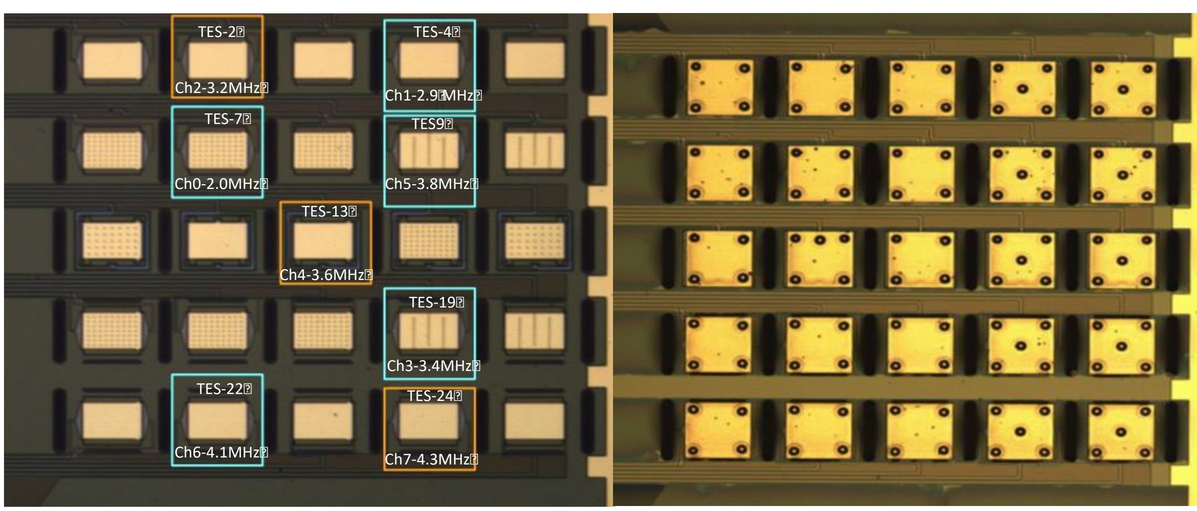

Fig. 3. a) TES numbers and their corresponding bias frequencies under FDM. b) Absorber types on the top of the TESes.

Although these devices are fabricated by DRIE process, we still have only horizontal Si support structures. This is because the same masks as for the old wet etching process was used, while the D-RIE process for etching grid Si support structures has been developed in this program. This process is now mature and reliable and will be used in the future fabrication runs. The thermal isolation between the devices in each row is implemented by vertical slots in the SiN membrane. The devices in the first top three rows have relatively a higher thermal conductance (G) and last two rows in the bottom have a lower G, which is realized by having horizontal slots in the SiN membrane in addition to the vertical ones. As we can see there are number of bare TESes, TESes with metallic bars and a TES with metallic dots. All devices have the same absorber size (165x165 m^2) and thickness (3 μm) made of electroplated gold. All absorbers have 4 contact points to the substrate at the corners but the absorbers in the first two right columns have an additional contact point in the center of the TES (see Fig. 3b).

3. MEASUREMENT SETUP

All measurements were performed in a dilution refrigerator that can cool the TESes down to ~40 mK. TESes were characterized under AC bias using our frequency-division multiplexing (FDM) readout system (1–5 MHz) [3]. The frequency separation between neighbor resonators is 200 kHz. The TES array chip and key components of FDM readout were mounted in a low magnetic impurity copper bracket fitted into an Al shield (see Fig. 4).

The bracket also accommodates a heater, a thermometer and a Helmholtz coil. The heater and thermometer are used to regulate the temperature on the chip mount locally. The coil is for applying a uniform magnetic field on the TES array.

(a) (b)

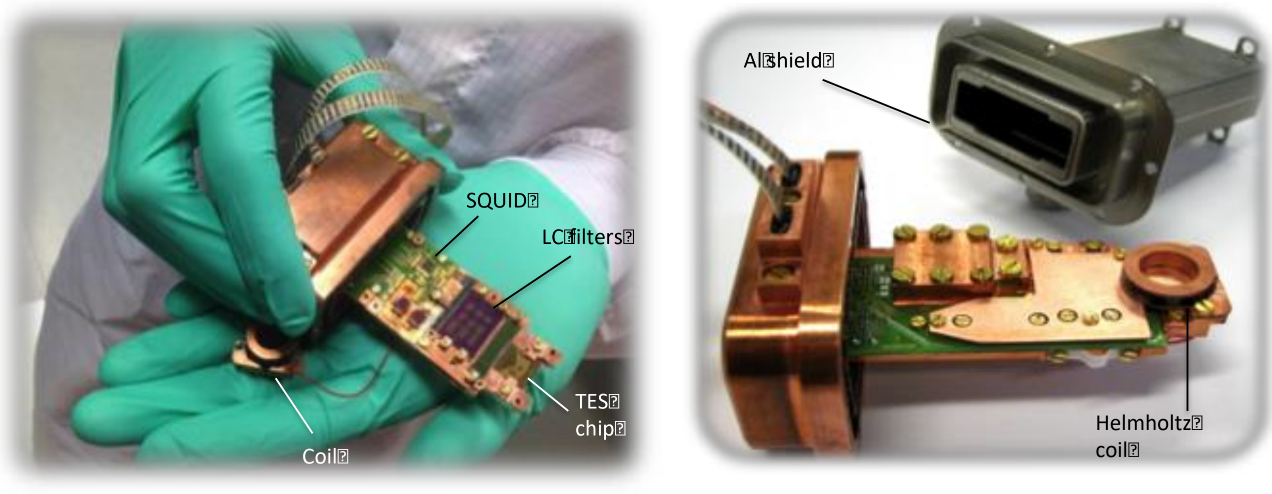

Fig. 4. (a) Picture of the copper bracket that holds the TES array, LC filter chip and the SQUID. (b) The chips were covered by thin copper sheets for protection and a Helmholtz coil was mounted on the top of the TES chip to apply a magnetic field. The whole bracket was then covered by an Aluminum (Al) shield.

4. MEASUREMENT RESULTS

4.1 TES Characterizations

For each TES pixel, we measured both in-phase and quadrature components of TES current, which are related to quasi-particle current that contributes to power dissipation in a TES and Josephson current, respectively [4]; the in-phase component of TES current was only used to characterize the TESes. I-V curves were taken at various bath temperatures and provide TES properties such as saturation power, thermal conductance and responsivity. The normal resistance (R_n) was obtained by measuring the quality factor (Q) when the TES was biased in the normal state. The response speed of the TES was measured by applying a small pulse to the bias line and recording the TES output signal. There are clear differences in the shape of the IV curves as shown below as an example. Some devices show fluctuating structure while some others are very smooth through out the transition. In general devices with bare TES are faster and therefore it is not possible to measure the IV curves very low in the transition.

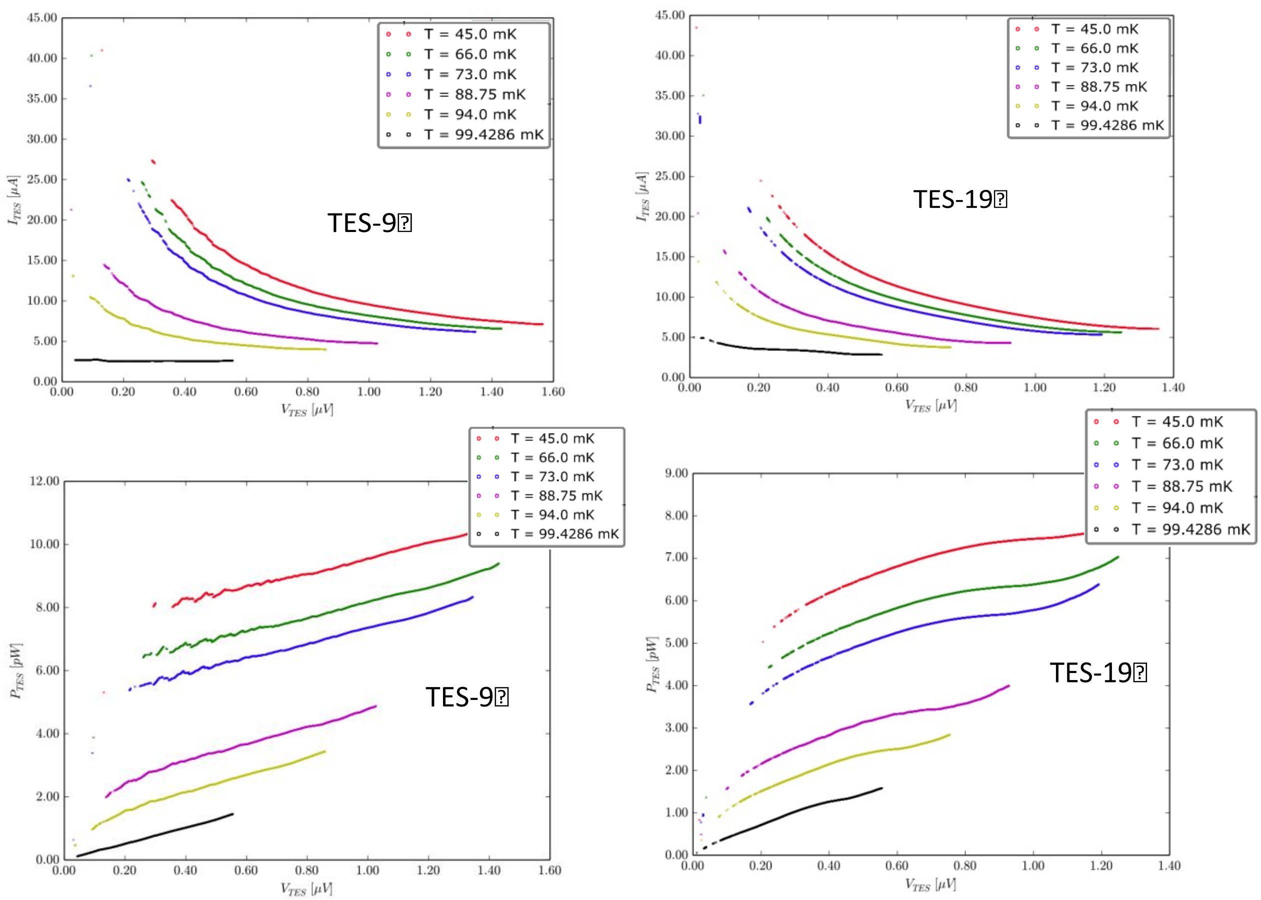

Fig. 5. IV and PV curves for TES-9 and TES-19. They both have the same metallic bars and absorbers but TES-9 has a lower G than TES-19.

The critical temperature of these TESes are in 100-105 mK range with normal resistance of around 250-260 mΩ. The thermal conductances are about 310-365 pW/K for high *G* devices and about 190-260 pW/K for low *G* ones. We measure saturation powers of about 8-10 pW for high *G* devices and about 5-7 pW for the low *G* ones.

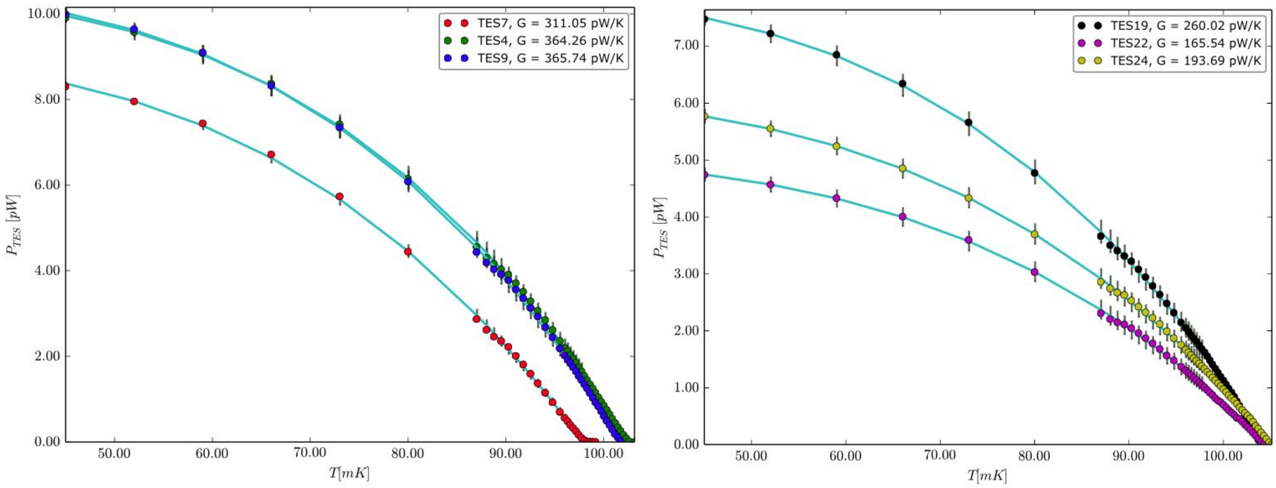

Fig. 6. Power vs. Temperature curves for 2–slot devices (left) and 4-slot devices (right).

Table 2 shows an overall comparison of our device parameters with LPA2 requirements (in green) for the X-IFU instrument [5]. TES-19 (in red) has the best energy resolution. In general our devices are by a factor of 2-4 faster than what is required. The same is valid for our *G* values. The effective time constants mentioned in the table are where the devices show the lowest noise and NEP, which is not necessarily at the same point in the transition for all devices. Slowing down the devices can be achieved by making the TES smaller. It is also possible to reduce he SiN thickness that is currently 1 µm. Since the 4-slot devices show lower *G*, we can also tune the thermal conductance by changing the slot size in the SiN.

Table 2. Comparison of the TES parameters with the guideline specifications from X-IFU

Parameter	LPA2	TES4	TES7	TES9	TES19	TES22	TES24
Heat capacity, C	0.80 pJ/K	0.6	0.6	0.6	0.6	0.6	0.6
Bath conductance, Gb	115 pW/K	371	313	375	264	170	200
Temperature exponent, n	3	3.63	3.4	3.62	3.49	3.56	3.44
Set-point temperature, T0	90 mK	102.4	97.8	101.7	104.6	104.4	105.3
Power, P0	2.7 pW	10	8.3	10	7.5	4.7	5.7
Effective thermal time constant t_{eff}	788 µs	140	250	400	450	230	270

4.2 Electrical Noise Equivalent Power

The noise equivalent power (NEP) was estimated at different biased points by measuring the noise current and the pulse response. We typically average 200-300 noise events (with no pulses) and 20-30 pulse events to calculate the current noise spectra and the FFT of the pulse response. Knowing the energy of the pulse (Fe-55 source used) and dividing the noise spectra by the responsivity gives us the NEP spectra. Integrating the NEP spectra gives us the baseline resolution that is reported in Fig. 7. The NEPs were also measured at couple of magnetic fields but the best results were achieved at zero magnetic field and that is what is reported here. At first glance it appears that many of the devices perform similarly and give about 3.5-4 eV baseline resolutions (see Fig. 7a). TES-19 stands out scoring below 3 eV at multiple bias points. It is a low *G* device with 4-slots in SiN and has metallic bars on the TES. The absorber has 5 connection points with one in the middle of TES that is also sitting on the middle metallic bar. TES-2 has exceptionally high noise. TES-13 with metallic dots and smooth IV curves has an exceptional small bias range that exhibits very high noise.

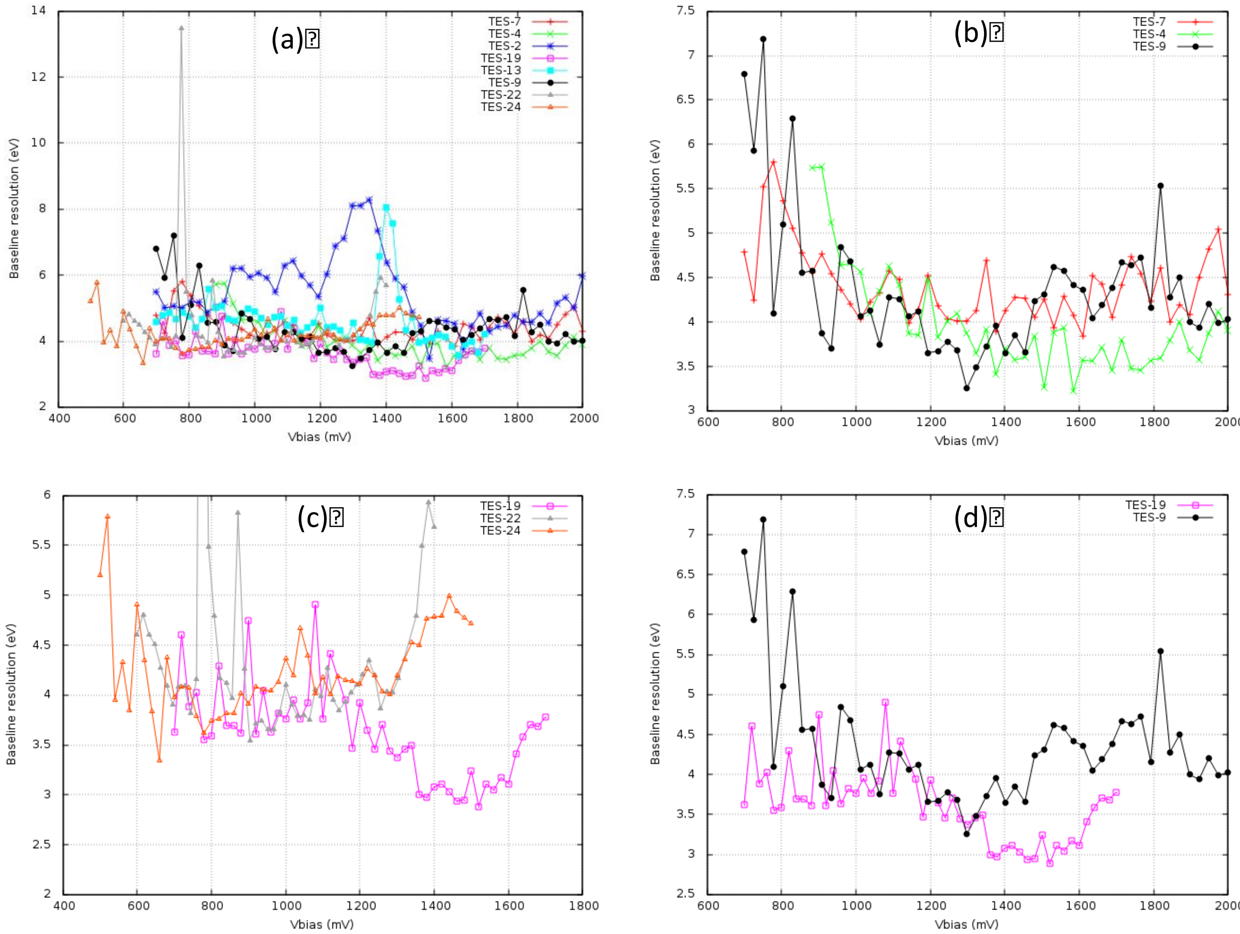

Fig. 7. Measured baseline resolution (based on NEP) as a function of the bias voltage. a) All 8 TESes. b) High G devices with 2-slots. c) Low G devices with 4-slots. d) Comparing TES-19 and TES-9. These two are identical in every aspect except for the G.

The background magnetic field was cancelled by applying 168 µA of current to the coil that corresponds to 3.8 µT magnetic field. Fig. 8 shows the NEP measurement for TES-19 as a function of bias point at different magnetic field. Applying ±7 µT does not change the base-line resolution drastically.

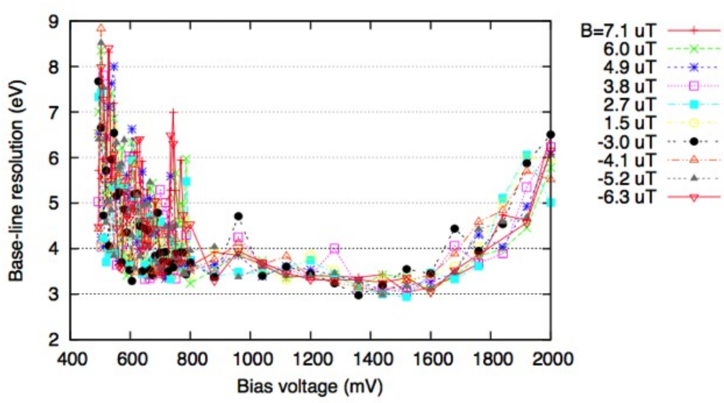

Fig. 8. Measured baseline resolution (based on NEP) at different magnetic field for TES-19. A fine scan around the zero background field did not improve the measured NEP.

4.3 X-ray Energy resolution

Measuring the NEP over a wide bias range identifies the promising operating points where good energy resolution can be expected. We measured 3.9 eV X-ray resolution at 6 keV with over 6300 counts, using TES-19 where baseline resolution was 2.9 eV (see Fig. 9). In this bias point the phase starts showing some steps possibly due to weak-link effect [6] and as we go down in the transition, these steps get larger. Other devices showed energy resolution between 4-5 eV at 6 keV.

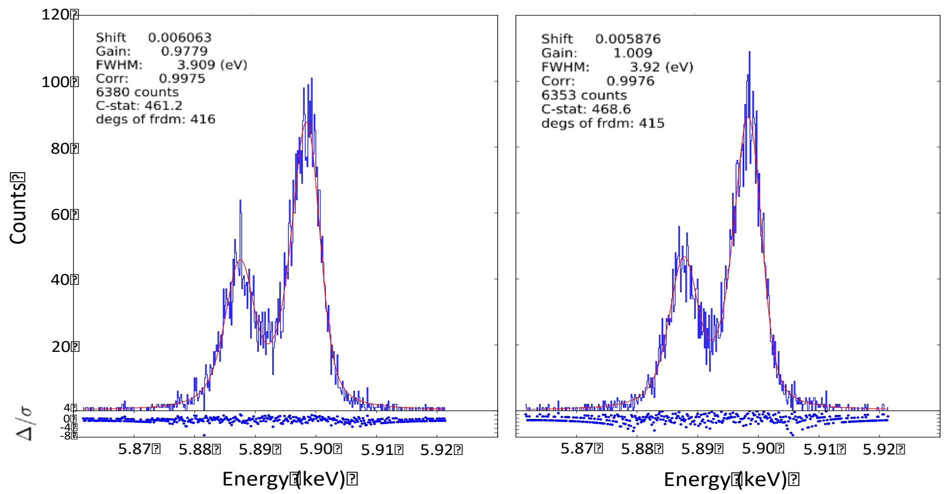

Fig. 9. X-ray resolution for TES-19 at two different bias points with over 6300 pulse counts.

The difference between the measured baseline and X-ray resolution is due to the stability of our measurement setup, which is not yet optimized for extremely accurate energy resolution measurement. Temperature drifts in warm electronics that cause slight gain drifts in the readout system should be minimized. Also our bath temperature fluctuation is currently at around 3-4 µK level. In order to measure energy resolutions of below 3 eV reliably, it is necessary to lower the thermal fluctuations to below 0.5 µK. This has been experimentally demonstrated on other setups at SRON by using SiG thermometers [3].

4.4 TES with full-size absorbers

The results presented so far is achieved using TESes with absorbers that are 3 µm thick gold with 165×165 µm^2 size. These are not representative for a final pixel design, as about 3-4 µm Bi layer must be added on the top the gold to enhance the absorbing efficiency. Besides, the size of the absorber must be increased to a full-size to cover more than 95% of the focal plane. The same TESes with full size absorbers have been fabricated and tested. This makes it possible to compare identical detectors with two different absorber types and show how a full-size absorber with Au and Bi perform compared to smaller Au absorbers (see Fig. 10).

(a) (b)

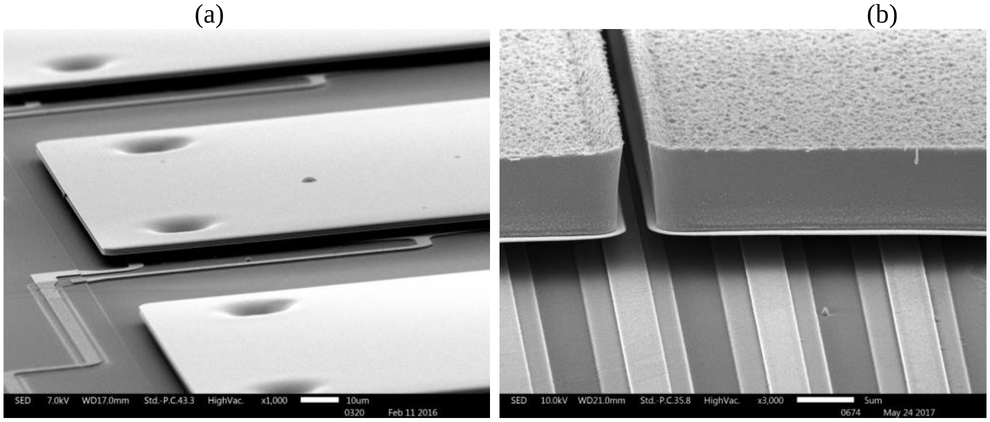

Fig. 10. (a) Half size (165×165 µm^2) absorbers with 3 µm Au. (b) Full-size (240×240 µm^2) absorbers with 3 µm Au and 3.5 µm Bi.

Ten devices were wired this time (see Fig. 11) to be measured using the FDM readout. We made sure that we have similar device designs covered for one to one comparison with the previous run. Especially, we measured four devices with metallic bars included that had the best performance before.

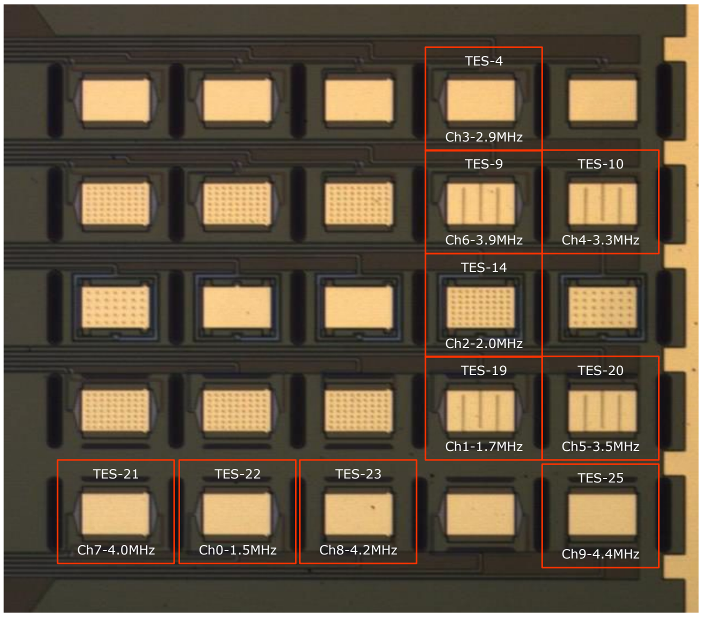

Fig. 11. a) TES numbers under test and their corresponding bias frequencies under FDM readout. These devices have Full-size (240×240 μm^2) absorbers with 3 μm Au and 3.5 μm Bi.

Similar to the previous run the NEP scans showed that the devices with metallic bars have lower noise with low *G* TESes (TES-19 and TES-20) showing baseline resolution as low as 3.5 eV (Fig. 12).

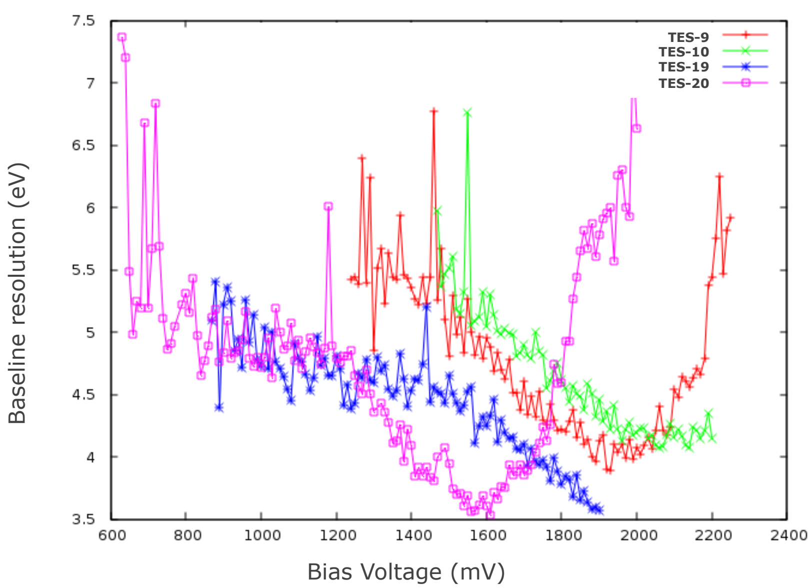

Fig. 12. Baseline resolution as a function of the bias voltage for four TESes with metallic bars. TES-9 and TES-10 are high G devices while TES-19 and TES-20 are low G.

Unfortunately the energy resolution measurements on all devices that have Au/Bi full-size absorbers show low energy tails in the spectra, similar to what is shown in Fig. 13. This was not seen in any of the devices with half-size Au absorbers.

This is most likely associated with the quality of Bi that can be estimated by measuring the residual resistivity ratio (RRR). Bismuth with RRR close to 1 has a semi-metal behaviour, which is considered good as an absorber. Bismuth with RRR < 0.5 has a semiconductor behaviour and can cause such low energy tails in the spectra [7].

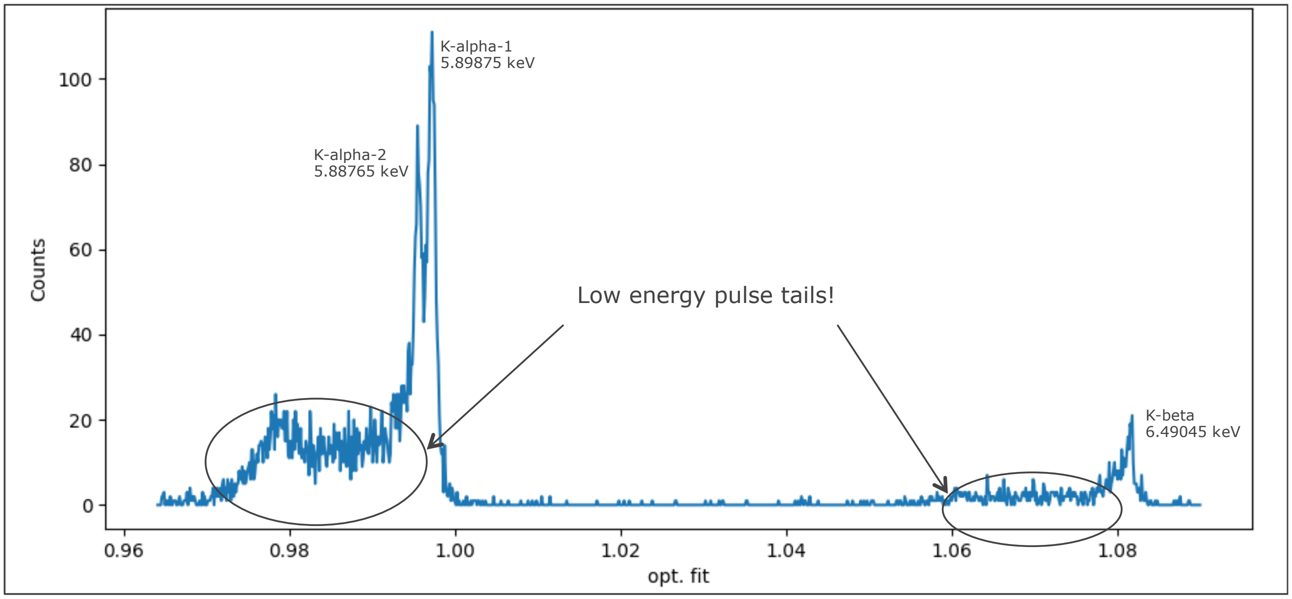

Fig. 13. An example of low energy tails, present in the measured spectra of Fe-55 X-ray source using all our devices with Au/Bi full-size absorbers.

5. SUMMARY AND DISCUSSIONS

It is clear that more devices should be measured before reaching an optimum design for our calorimeter. Variation is TES size has to be explored. The current TES size is too big (100×140 μm^2) and experience with Goddard devices shows that it is more likely to achieve better energy resolution with smaller size TESes (50×50 to 80×80 μm^2), where IV curves are smoother and has less structures [8]. Since the heat conductance (G) is proportional to the perimeter of the TES, smaller devices will be slower and help us to get closer to the desired speed. It is also encouraging that our best results so far are from low-G devices so lowering the G further might lower the over all noise as well.

Our devices so far only have vertical Si bars and the next fabrication runs will have grid Si support structure that is needed for large arrays. This is likely to increase the G to some extend (less than factor of 2), which can be compensated by reducing the membrane thickness. The SiN thickness is currently 1 μm and can be safely reduced to 0.5 μm. As we know from experience with bolometer TESes, reducing the heat capacity of the thermal link between the TES and the bath reduces the thermal fluctuation noise [9]. Therefore thinning the SiN is also likely to reduce the noise too. If the TESes become too slow, we can have the full membrane with no slots.

Presence of the metallic bars on the TESes with current size is essential for reducing the alpha and avoiding pulse saturation. Full size absorbers are about a factor of 2.2 larger and less prone to pulse saturation. However large heat capacity increases the noise and therefore in the new Au/Bi absorbers we will reduce the thickness of gold to 2 μm (currently is 3 μm). The best absorber coupling is with 5 contact points with the one in the center on a metallic bar so far. Experience with Goddard detectors shows that bars might not be needed on small TESes and one contact point is sufficient [10, 11]. Whether this is the case for SRON devices or not remains to be seen. From our devices so far we see that metallic dots lower the alpha and the speed but not the noise. This also needs to be confirmed by measuring more such devices.

The current TES resistance is above 200 mΩ and too high. It is worthwhile to explore the performance of the TESes with lower resistance. The resistance will immediately go down by a factor of 1.4 by choosing a square TES geometry (currently TESes are rectangular 140×100 μm^2). Tuning the Ti/Au thicknesses in the bilayer can further reduce the resistance. This is likely to reduce the noise too as Goddard detectors with very low energy resolution have very low normal resistances (R_n=10 mΩ) [12, 13].

The *Tc* of our devices is around 100 mK and higher than the X-IFU requirement (i.e. 90 mK). Tuning the device resistance will be combined with reducing the *Tc* to 90 mK, which also reduces the noise. We choose a 24/114 nm of Ti/Au bilayer for the next fabrication run. Our expectation is that it gives a *Tc* of about 90 mK and a $R_\square$ of about 80 mΩ.

Taking all the above discussions in to account for the 80×80 μm^2 TES the *G* is expected to go down by a factor of 2.5 to around 100 pW/K and larger and thinner absorber will increase the *C* to around 0.8 pJ/K, which are the desired values for X-IFU instrument.

In order to address the Bi problem without hindering the progress on the other aspects, we have decided to follow two parallel routes: In the next fabrication run we only use large Au absorbers. While these devices are being tested, we will try to improve our electroplated Bi quality and once acceptable RRR of the representative layer is achieved, another batch of devices with Au/Bi absorbers will be fabricated.

6. ACKNOWLEDGEMENTS

This work is partly funded by European Space Agency (ESA) and coordinated with other European efforts under ESA CTP contract ITT AO/1-7947/14/NL/BW. It has also received funding from the European Union's Horizon 2020 Programme under the AHEAD (Activities for the High-Energy Astrophysics Domain) project with grant agreement number 654215.

REFERENCES

1. European Space Agency (ESA), "ATHENA Mission Summary", Available: http://sci.esa.int/athena/59896-mission-summary/. [Accessed: Jul. 6, 2018]
2. D. Barret et al., "The Athena X-ray Integral Field Unit (X-IFU)", Proc. SPIE 9905, 99052F (2016); https://doi.org/10.1117/12.2232432
3. H. Akamatsu et al, "Development of frequency domain multiplexing for the X-ray Integral Field unit (X-IFU) on the Athena", Proc. SPIE 9905, 99055S (2016); https://doi.org/10.1117/12.2232805
4. L. Gottardi et al, "Josephson effects in an alternating current biased transition edge sensor", Appl. Phys. Lett. 105, 162605 (2014); https://doi.org/10.1063/1.4899065
5. R. den Hartog et al, "Requirements for the detectors and read-out of ATHENA X-IFU", Proc. SPIE 9144, 91445Q (2014); https://doi.org/10.1117/12.2056434
6. L. Gottardi et al, "Weak-Link Phenomena in AC-Biased Transition Edge Sensors", J Low Temp. Phys. 176, 3 (2014); https://doi.org/10.1007/s10909-014-1093-9
7. D. Yan et al, "Eliminating the non-Gaussian spectral response of X-ray absorbers for transition-edge sensors", Appl. Phys. Lett. 111, 192602 (2017); https://doi.org/10.1063/1.5001198
8. K. Sakai et al, "Study of Dissipative Losses in AC-Biased Mo/Au Bilayer Transition-Edge Sensors", J Low Temp Phys (2018); https://doi.org/10.1007/s10909-018-2002-4
9. P. Khosropanah et al, "Ultra-low noise TES bolometer arrays for SAFARI instrument on SPICA", Proc. SPIE 9914, 99140B (2016); doi: 10.1117/12.2233472
10. S.J. Smith et al, "Transition-edge sensor pixel parameter design of the microcalorimeter array for the x-ray integral field unit on Athena", Proc. SPIE 9905, 99052H (2016); https://doi.org/10.1117/12.2231749
11. S.J. Smith et al, "Transition-edge sensor array development for the ATHENA x-ray itegral field unit", In this SPIE proceeding (2018).
12. L. Gottardi et al, "Study of TES-Based Microcalorimeters of Different Size and Geometry Under AC Bias", IEEE Trans. Appl. Supercond (Volume: 27, Issue: 4, June 2017); https://doi.org/10.1109/TASC.2017.2655500
13. L. Gottardi, et al, "Josephson Effects in Frequency-Domain Multiplexed TES Microcalorimeters and Bolometers", J Low Temp Phys (2018); https://doi.org/10.1007/s10909-018-2006-0